Energy & Environmental Science

High-capacity thermochemical CO2 dissociation using iron-poor ferrites

Journal:	*Energy & Environmental Science*
Manuscript ID	EE-ART-08-2019-002795.R1
Article Type:	Paper
Date Submitted by the Author:	10-Dec-2019
Complete List of Authors:	Zhai, Shang; Stanford University, Mechanical Engineering Rojas, Jimmy; Stanford University, Mechanical Engineering Ahlborg, Nadia; Stanford University, Materials Science & Engineering Lim, Kipil; Stanford Synchrotron Radiation Lightsource, Materials Science Cheng, Michael ; Harvard University, Physics Xie, Chenlu; Stanford University, Mechanical Engineering Toney, Michael; Stanford Synchrotron Radiation Laboratory, Jung, In-Ho; Seoul National University, Department of Materials Science and Engineering; Mcgill university, Department of Mining and Materials Engineering Chueh, William; Stanford University, Materials Science and Engineering Majumdar, Arunava; Stanford University, Mechanical Engineering

High-capacity thermochemical CO_2 dissociation using iron-poor ferrites

Shang Zhai[1,9], Jimmy Rojas[1,9], Nadia Ahlborg[2], Kipil Lim[2,3], Chung Hon Michael Cheng[4,5], Chenlu Xie[1], Michael F. Toney[3], In-Ho Jung[6], William C. Chueh[2,7,8,*], Arun Majumdar[1,7,*]

[1] Department of Mechanical Engineering, Stanford University, Stanford, CA 94305, USA

[2] Department of Materials Science and Engineering, Stanford University, Stanford, CA 94305, USA

[3] Stanford Synchrotron Radiation Lightsource, SLAC National Accelerator Laboratory, Menlo Park, CA 94025, USA

[4] Department of Physics, Harvard University, Cambridge, MA 02138, USA

[5] John A. Paulson School of Engineering and Applied Sciences, Harvard University, Cambridge, MA 02138, USA

[6] Department of Materials Science and Engineering, Seoul National University, Seoul, 08826, South Korea

[7] Precourt Institute for Energy, Stanford University, Stanford, CA 94305, USA

[8] Applied Energy Division, SLAC National Accelerator Laboratory, Menlo Park, CA 94025, USA

[9] These authors contributed equally

[*] Corresponding authors: wchueh@stanford.edu; amajumdar@stanford.edu

Abstract

Dissociation of CO_2 to form CO can play a key role in decarbonizing our energy system. We report here a two-step thermochemical cycle using a variety of iron-poor (Fe-poor) ferrites ($Fe_yM_{1-y}O_x$ where $y < 2/3$) that produces CO with unusually high yield using Fe as the redox active species. Conventional wisdom suggests that increasing the Fe fraction would increase the capacity for CO_2 dissociation. Here, we report the opposite result: at partial pressure ratio $CO:CO_2 = 1:100$, we demonstrated the CO yields of 8.0 ± 1.0 mL-CO/g from $Fe_{0.35}Ni_{0.65}O_x$, and 3.7 ± 1.0 mL-CO/g from $Fe_{0.45}Co_{0.55}O_x$, at a thermal reduction temperature of 1300°C; remarkably, these CO_2 dissociation capacities are significantly higher than those of state-of-the-art materials such as spinel ferrites (Fe_2MO_4), (substituted) ceria, and Mn-based perovskite oxides. Optimization of kinetics of Fe-poor ferrites with ZrO_2 support resulted in higher CO yields per gram of ferrite. The unexpected CO yield vs. Fe ratio trend is consistent with the prediction of calculated ternary phase diagrams, which suggest a swing between spinel and rocksalt phases. These Fe-poor ferrites open new opportunities for tuning redox properties of oxygen exchange materials.

Key Words

CO_2 dissociation, thermochemical, Fe-poor ferrite, ternary system

Broader context

The ability to dissociate CO_2 to produce CO is vitally important in energy sciences because it would enable synthetic transformation of CO_2 into chemicals and fuels. The potential broad impact of this reaction to decarbonize the global energy system will only be fully realized when this occurs at the Gigatonne scale. Today's chemical infrastructure at this scale relies exclusively on *thermochemical transformations*, which warrants research in identifying materials for thermochemical CO_2 dissociation. We report here the discovery of a previously unexplored regime of iron-poor ferrites with lower Fe concentration than the traditionally investigated spinel ferrites for two-step thermochemical CO_2 dissociation. The Fe-poor composition induces spinel-rocksalt phase transitions, which increases the CO_2 dissociation capacity by a factor of 2 to as high as 10 compared to state-of-the-art materials such as spinel ferrites, ceria and perovskites. Predictions based on calculated phase diagrams can explain the experimental observations, further confirming the role of controlling phase transitions involving Fe^{2+} to Fe^{3+}. Preliminary studies on kinetics suggest that use of zirconia supports for Fe-poor ferrites can significantly increase reactions rates. Our discovery opens a new direction of scientific inquiry in redox thermochemistry as well as the opportunity for scalable CO_2 dissociation.

1. Introduction

Approximately 40 Gt-CO_2 is emitted per year globally, half of which accumulates in the atmosphere and contributes to global warming[1,2]. There are worldwide efforts to reduce net greenhouse gas (GHG) emissions and hold "the increase in global average temperature to well below 2°C above pre-industrial levels"[3–8]. One approach to achieve this goal is the synthetic transformation of CO_2 into chemicals and fuels, which could offer the potential for emission reductions and even negative emissions[2,9–13]. For these to make a difference to global warming, the processes need to be cost-competitive with current approaches to synthesize chemicals and fuels and compatible for scale-up in an infrastructure capable of handling Gt-scale CO_2. Many researchers have investigated electro-[14–17] and photo(electro)-catalysts[18–20] for CO_2 reduction and, more broadly, artificial photosynthesis[21–23] pathways for solar-fuel production. While they have advantages such as flexibility, mild condition and reasonably high efficiency[17,18], it is noteworthy that the chemical infrastructure today at the Gt-scale relies almost exclusively on thermochemical processes. Hence, such dominance of thermochemistry warrants research in creating options for the thermochemical reduction/hydrogenation of CO_2[24–30] by carbon-free heat/hydrogen, although they have received comparatively less attention. The key motivation of this paper, therefore, is to identify materials, the thermodynamic mechanisms, and the capacity limit for reducing CO_2 in a two-step Thermochemical Carbon Dioxide Dissociation (TCDD) cycle[31–38]. Meanwhile, the authors acknowledge the challenges facing many TCDD materials, such as high operational temperature and limited conversion[27]; on the other hand, our previous study[39] and the current paper are aiming at tackling these challenges.

In a two-step cycle, a metal oxide (MeO_x) is first reduced at a high temperature, T_H, and at a specific oxygen partial pressure (pO_2)

$$\text{Thermal Reduction step at } T_H\text{: } MeO_x \rightarrow MeO_z + \frac{(x-z)}{2}O_2 \quad (1)$$

Next, the reduced oxide is exposed to CO_2 at a lower temperature, T_L, during which part of the supplied CO_2 can be converted to CO

$$CO_2 \text{ Splitting step at } T_L\text{: } MeO_z + (x-z)CO_2 \rightarrow MeO_x + (x-z)CO \quad (2)$$

Oxides for such cycles mainly fall into two mechanistic categories[27]: single-phase materials (e.g., $CeO_{2-\delta}$ [33,36,38,40], perovskites[41–47]) and phase change materials (e.g., spinel ferrites Fe_2MO_4, where M can be one or mixed metals[48–54]).

In a fed-batch system, CO product accumulates in the reactor during Reaction (2), thereby imposing a background partial pressure of CO. After CO_2 splitting at a specific condition, there exists a critical background partial pressure ratio of CO versus CO_2 (referred to as $CO:CO_2$) at T_L at which the metal oxides go from gaining oxygen to losing oxygen[47]. A high critical pressure ratio is desirable since it implies a high driving force for Reaction (2) for net CO production, and directly translates to a higher CO_2 to CO conversion[55,56]. However, it has been challenging to identify materials that can perform two-step TCDD at a high critical ratio. Many previously explored materials give either small or negative yields of CO when considering $CO:CO_2 = 1:100$ at $T_H \leq 1300°C$, leading to high required operation temperatures. For many perovskite oxides (e.g., $LaMnO_{3-\delta}$ family)[42,44–46,57,58], the material can readily evolve oxygen at modest temperatures, but the thermodynamics of Reaction (2) is such that the driving force for CO_2 splitting is low. For example, when thermal reduction is at $T_H = 1300°C$ and $pO_2 = 10^{-5}$ atm, and CO_2 splitting $T_L = 800°C$, $La_{0.8}Sr_{0.2}MnO_{3-\delta}$ has a critical $CO:CO_2 = 1:250$, and its thermodynamic equilibrium CO yield is only 0.8 mL/g if $CO:CO_2 = 1:1000$; additionally, for $La_{0.6}Sr_{0.4}MnO_{3-\delta}$, the critical $CO:CO_2 = 1:650$ and the equilibrium yield is 1.1 mL-CO/g at $CO:CO_2 = 1:1000$. (See **Electronic Supplementary Information (ESI)** and previous work on thermodynamic diagrams[45] and equilibrium CO yield calculation[39].)

Early work on Fe_3O_4-FeO redox couple[24,59–62] targeted high capacity for CO_2 dissociation (and/or H_2O dissociation, which are similar in a two-step thermochemical cycle[31]) through complete phase transformation, and required extremely high temperature (usually above 1700°C) that can melt/vaporize and thus deactivate the oxides. To alleviate the problem of melting/vaporizing, substituted ferrites ($Fe_yM_{1-y}O_x$) have been extensively explored for two-step TCDD at lower temperatures[49,63–66]. Additionally, support materials such as ZrO_2 have been used to improve reaction activity and cyclability of ferrites[67–70]. Nonstoichiometric ferrite processes were also explored but gave very limited capacity because of the small magnitude of nonstoichiometry in spinel-type ferrites[24,71]. To the best of our knowledge, such studies have focused on materials where the iron fraction is kept greater than two-thirds ($y > 2/3$). Materials with iron fractions substantially less than two-thirds contain a substantial

fraction of rocksalt phase. Conventional wisdom[54] implied in all the studies suggests that having the reduced rocksalt phase in the as-synthesized compound (typically in air) will lead to poor CO production capacity. Hence, the Fe-poor ferrites have remained largely unexplored for thermochemical cycles.

Here, we challenged this conventional wisdom and synthesized compounds containing a significant fraction of reduced material (rocksalt phase) under oxidizing conditions. We increased the ratio of substitute metal(s) and obtained "Fe-poor" ($y < 2/3$) two-phase ferrites[72–74] with significantly superior performance under our cycling conditions. In such a two-phase system, partial phase transformation between spinel and rocksalt phases decomposes CO_2 into CO and O_2, and the compositions of both phases evolve during such oxygen exchange cycles. Our previous work demonstrated high H_2-production capacity during water splitting in an "Fe-poor' oxide with high mixing entropy [39]. In this work, we show that high CO yields can be obtained in simpler, ternary systems if the Fe mole fraction is optimized. Furthermore, we show that the optimal y in $M_{1-y}Fe_yO_x$ is always in the "Fe-poor" regime ($y < 2/3$) for M = Co, Ni, or Mg. Additionally, we present a method to improve the kinetics of both reaction steps by ZrO_2. Preliminary results show an increase of CO yield per gram of ferrite compared to pure ferrites for limited reaction time, and it provides a path towards the reduction of cycle time from hours to minutes.

2. Results and Discussion

2.1 Improved performance of Fe-poor ferrites in two-step thermochemical CO_2 dissociation

The sol-gel technique was used to synthesize a series of ferrite samples, among which $Fe_{0.35}Ni_{0.65}O_x$ particles of ~0.2 μm and $Fe_{0.45}Co_{0.55}O_x$ particles of ~1 μm were produced (**Figs. S1A** and **S1B**). The size difference is likely due to difference in the degree of sintering. The two-step TCDD cycles were conducted in a customized thermogravimetric analyzer (TGA) setup connected to a carbon monoxide (CO) sensor, as shown in **Fig. S2**. Sample thermal reduction was achieved at T_H with Ar purging ($pO_2 = 5 \sim 20$ ppm); then the furnace was cooled to T_L before introducing a mixture of CO_2 and CO (in Ar). Both CO and CO_2 concentrations were specified to give the driving force not only for the CO_2 to CO forward reaction but also for the reverse reaction (CO oxidation by the oxide).

A series of Fe-poor ferrites $Fe_yM_{1-y}O_x$ with M = Ni, Co and Mg were measured. The conditions were T_H = 1300°C and T_L = 800°C; dwell time at both steps was 5 hours each; during CO_2 splitting step, CO:CO_2 = 1:100. As shown in **Figs. 1A, 1B** and **S3B**, the concentration, y, of Fe is a significant factor in determining CO_2 dissociation performance; y = 0.667 corresponds to traditionally explored spinel ferrites MFe_2O_4. In $Fe_yNi_{1-y}O_x$ system, y = 0.35 was found to be the optimal composition, corresponding to CO production of 8.0 ± 1.0 mL-CO/g, which is about six times the thermodynamic limit of CO production by CeO_{2-X} under the same reaction conditions, whereas $La_{1-x}Sr_xMnO_{3-\delta}$ (x = 0.2, 0.3, 0.4) materials would have negative CO productions as discussed earlier, thus not shown in the figures mentioned above (a more complete comparison of thermodynamic capacities can be found in **Table 1**). In the $Fe_yCo_{1-y}O_x$ system, the optimal measured value was y = 0.45 with a CO production of 3.7 ± 1.0 mL-CO/g. Under the same temperature conditions of T_H = 1300°C and T_L = 800°C, when we relaxed the requirement to be CO:CO_2 = 1:1000 for Reaction (2), both $Fe_{0.35}Ni_{0.65}O_x$ and $Fe_{0.45}Co_{0.55}O_x$ showed yield of about 15 mL-CO/g, which is ten times higher than thermodynamic limit of CeO_{2-X} (**Fig. 1C**).

We define "Fe redox limit" (in mL-CO/g) as the CO yield if all the Fe atoms in a ferrite went through +2/+3 redox in a two-step TCDD cycle; in the calculation, the ferrite formula weight was determined by setting Fe, Mg, Co and Ni at oxidation states of +3, +2, +2 and +2, so that the "Fe redox limit" is independent of reaction conditions (See **Table S1**). The measured yield normalized by the corresponding Fe redox limit of a ferrite, which indicates the portion of Fe that is redox active at a specific test condition, was plotted as "normalized yield" in **Figs. 1A-C** and **S3B**. For instance, under T_H = 1300°C, T_L = 800°C and CO:CO_2 = 1:100, $Fe_{0.35}Ni_{0.65}O_x$ showed the best normalized yield of 15.6 ± 2.0 % among all tested materials; changing CO:CO_2 to 1:1000 made its normalized yield increase to 28.9 ± 2.0 %. The dependence of normalized CO yield on Fe concentration followed a similar trend to that of absolute yield (in mL-CO/g). Both these figures of merit showed that redox activity of Fe reaches optimum far from y = 2/3. On the other hand, if we define "normalized yield" similarly for CeO_2 as the ratio of cerium that is redox active for certain reaction condition, its normalized yield is only 2.1% under T_H = 1300°C and pO_2 = 10 ppm, and T_L = 800°C and CO_2:CO = 100:1.

Shorter cycles with T_H = 1300°C, T_L = 800°C and CO:CO_2 = 1:100 showed cyclability of $Fe_{0.35}Ni_{0.65}O_x$, $Fe_{0.45}Co_{0.55}O_x$, and $Fe_{0.35}Mg_{0.65}O_x$ (**Fig. S4**). The dwell time for both thermal

reduction and CO_2 splitting steps was 1 hour each. In the first few cycles, CO yields were low because of the relatively slow reaction rate: The oxygen uptake from CO_2 was smaller than the oxygen loss in the preceding thermal reduction, before finally establishing periodic oxygen content swing after the initial cycles. This can be demonstrated by the thermogravimetric curves along with CO profiles in **Fig. S5**. Fortunately, the CO production yield of the three materials did not monotonously decay within 10 cycles, but the yield did show some fluctuations. We recognize that it requires tens of thousands of cycles to prove feasibility for industrial application, which is a topic of a later study. The particle sizes grew from ~1 μm to ~10 μm after 10 cycles (**Figs. S1C** and **S1D**).

While the goal of this paper is to demonstrate thermodynamic feasibility and CO_2 dissociation capacity, we explored the kinetics to some degree as well. **Fig. 1D** contains the CO concentration profiles during CO_2 splitting step for $Fe_yNi_{1-y}O_x$ materials with T_H = 1300°C (5 hours long), T_L = 800°C and CO:CO_2 = 1:100 condition. The background profile was for a test with the same condition but without a sample in the TGA. CO yield values were calculated by subtracting the background CO profile from the profile during a sample test. $Fe_{0.45}Ni_{0.55}O_x$ exhibited the highest peak rate of CO production (a rough measure of kinetic performance); meanwhile, both $Fe_{0.45}Ni_{0.55}O_x$ and the pure spinel, $NiFe_2O_4$, exhibited an initial steep increase of CO. The stable level of CO for the test of $NiFe_2O_4$ was lower than the background, which may be due to catalysis of CO combination with background O_2 (5~20 ppm) by $NiFe_2O_4$. Overall, CO evolution finished more than 60% within 1 hour and exhibits a long tail. The slow kinetics may be from bulk transport of lattice oxygen in the solid and the insufficient gas-solid contact inside the TGA. Quantitative kinetics are explored as well.

A mixture of $Fe_{0.35}Ni_{0.65}O_x$ with ZrO_2 was found to improve the kinetics of the process as shown in **Fig. 1E**; a similar strategy has been shown in previous work[49,69,70]. Bare ZrO_2 had been tested to show no activity in either thermal reduction step under T_H = 1300°C and pO_2 = 10 ppm, or CO_2 splitting step under T_L = 800°C and CO_2:CO = 100:1. Improvement in kinetics was demonstrated by conducting reactions with shorter time (1 hour per step instead of 5 hours per step in **Figs. 1A-D**). Adding ZrO_2 resulted in better CO production performance. With the limited reaction time, the CO yield per gram of ferrite increased to more than twice and the multi-cycle performance seems to be more stable compared to iron-poor ferrites without ZrO_2. Additionally, the $Fe_{0.35}Ni_{0.65}O_x$-ZrO_2 (80% ZrO_2 mass fraction) had been tested with 5-hour long thermal reduction at T_H = 1300°C and pO_2 = 10 ppm, and 5-

hour long CO_2 splitting at T_L = 800°C and CO_2:CO = 100:1. The purpose of this long thermal reduction and CO_2 splitting steps was to achieve equilibrium. Indeed, we found that under such conditions, it produced the same amount of CO per gram of ferrite compared to $Fe_{0.35}Ni_{0.65}O_x$ (8.0 ± 1.0 mL-CO/g) without the use of ZrO_2. Hence, the use of ZrO_2 did not change the thermodynamics, but rather only the kinetics. In fact, the ZrO_2 supported ferrite reached the CO yield within 70 min after CO_2 splitting step started, compared to ~20 hours equilibration time without ZrO_2 support, indicating that reaction rate was significantly improved by ZrO_2. Furthermore, morphology characterization and elemental mapping have shown that ZrO_2 can separate particles of ferrites and lower the degree of sintering: after 10 cycles, the separated ferrite has size of ~1 μm (**Fig. S1H**), compared to ~10 μm (**Fig. S1C**) without ZrO_2. Thus, the improved kinetics can be from the facile mass and heat transfer due to the reduced particle size of the ferrite. The complete mechanism of kinetics improvement is worth further research.

2.2 Rocksalt-spinel phase swing and Fe redox

The degree of phase transition in the Fe-poor ferrites was investigated by x-ray diffraction (XRD) on $Fe_{0.35}Ni_{0.65}O_x$ and $Fe_{0.35}Co_{0.65}O_x$ quenched from thermal reduction and CO_2 splitting conditions. A sol-gel synthesized ferrite was quenched in Ar purge gas after 3 hours dwell for either thermal reduction (at T_H) or CO_2 splitting (at T_L) reaction. A quenched sample was assumed to have the same phase composition as it had at the end of the 3-hour reaction. In **Figs. 2A**, **S6** and **Table S2**, the spinel-rocksalt phase ratio changes can be clearly shown by Rietveld refinement, as well as their relative diffraction peak height. Specifically, thermally reduced ferrites exhibit more rocksalt phase compared to samples oxidized in CO_2, similar to traditional spinel ferrites. However, Fe-poor ferrites contain both phases throughout the two-step cycle, and the rocksalt phase is not a minority phase.

Performing x-ray absorption near-edge spectroscopy (XANES) on quenched samples, we found Fe is the redox active element in $Fe_{0.35}Ni_{0.65}O_x$ and $Fe_{0.35}Co_{0.65}O_x$. As **Figs. 2B** and **2C** show, the Fe-K edge energy shift (evaluated at normalized absorption of 0.5) of $Fe_{0.35}Ni_{0.65}O_x$ was 0.5 eV between thermally reduced state at 1300°C and CO_2 oxidized state at 800°C; the Fe K-edge shift for $Fe_{0.35}Co_{0.65}O_x$ was 0.4 eV (compared to 4.3 eV between Fe^{2+} and Fe^{3+} references). This edge shift roughly corresponds to the normalized yield of 15% in **Fig. 1A**. On the other hand, Co and Ni absorption edges did not change during the redox cycle,

indicating that they are redox inactive (**Fig. S9**). Since Fe is the redox active species, the possibility of lowering Fe for improving the capacity for CO_2 splitting is somewhat counterintuitive. We investigated this by calculating the phase equilibria of these ternary oxides.

2.3 Thermodynamic analysis

CALculation of PHase Diagram (CALPHAD) thermodynamic database was used for chemical equilibria analysis. The two most relevant oxide solutions in the present study are spinel solution and rocksalt solution. The spinel solution is described using the Compound Energy Formalism considering the crystal structure of solution, $(Fe^{2+}, Fe^{3+}, Co^{2+}, Co^{3+}, Mg^{2+}, Ni^{2+})^{T}[Fe^{2+}, Fe^{3+}, Co^{2+}, Co^{3+}, Mg^{2+}, Ni^{2+}, Va]_2^{O}O_4$, where T and O represent the tetrahedral sites and octahedral sites in the spinel solution and Va means vacancy in octahedral sites. Rocksalt solution is formulated as the solution of FeO-$FeO_{1.5}$-MgO-CoO-NiO-etc., where $FeO_{1.5}$ is considered to describe the non-stoichiometry of wustite. The metallic phases were taken from FSStel database in FactSage.

Models based on the CALPHAD equilibrium analysis of the $Fe_yM_{1-y}O_x$ system (M = Mg, Co, Ni) predicted thermodynamic equilibrium CO yield from $Fe_{0.35}Ni_{0.65}O_x$ to be 10.4 mL-CO/g at conditions of T_H = 1300°C, T_L = 800°C and CO:CO_2 = 1:100, which are shown as circles in **Fig. 3A**. Furthermore, elemental molar amount at thermodynamic equilibrium was predicted for both spinel and rocksalt phases. The total amount of metal cation was set as one mole without losing generality. As **Fig. 3B** shows, $Fe_{0.35}Ni_{0.65}O_x$ has phase swing between thermally-reduced and CO_2-oxidized states, and the difference in total molar amount indicated by dash line is the thermodynamic oxygen exchange capacity. Similarly, the predicted phase swing and oxygen exchange capacity can be shown for $Fe_{0.67}Ni_{0.33}O_x$ ($NiFe_2O_4$), $Fe_{0.45}Co_{0.55}O_x$ and $Fe_{0.67}Co_{0.33}O_x$ ($CoFe_2O_4$) as well (**Figs. S13-S15**). The predicted phase swing is larger for the two Fe-poor ferrites than the traditional "spinel" ferrites. Also, the elemental composition of each phase is noted with a formula, which changes with temperature and pO_2, but does not depend on the global Fe:M composition (See **Table S5**; compare **Fig. 3B** with **S14**, **S13** with **S15**) if within rocksalt-spinel two-phase region.

The CO yield dependence on Fe stoichiometry y for $Fe_yM_{1-y}O_x$ is in **Fig. 3C**. For different metals, M = Ni, Co and Mg, the optimal values of y were 0.29, 0.41 and 0.36, respectively.

The predicted trend of CO yield dependence on y here is consistent with measurements (**Fig. 1**), even though predicted equilibrium yields are generally higher than measured, which was limited by kinetics. Selected materials were tested for 20 hours of thermal reduction plus 20 hours of CO_2 splitting, and the measured CO yield is quantitatively consistent with the CALPHAD predictions (**Fig. 3C**).

The previously proposed thermodynamic framework[26,31] provides a means to visualizing the effect of global iron concentration on the redox capacity of the ferrites. **Fig. 4** shows the partial molar enthalpy (h_O) and entropy (s_O) of oxygen for the mixed-phase ferrites against the triangular shape regions thermodynamically feasible for both thermal reduction and CO_2 splitting reactions (analysis method is given in the **ESI**). Along the thermodynamics trajectory of each oxide in the plot, each symbol represents an oxygen content change of 0.005 mol of oxygen per mol of metal; the number of line segments that fall within the highlighted purple region of the triangle plot is proportional to the thermodynamically predicted oxygen swing (i.e. maximum fuel productivity). The insets of **Fig. 4A** show that decreasing the amount of iron in $CoFe_2O_4$ shifts the magnitude of partial molar enthalpy slightly down. The iron-poor composition also has a slightly higher horizontal density of symbols in the triangular region, indicating that the slope of partial molar entropy vs. oxygen content is slightly shallower. **Fig. 4B** shows that in the Fe-Ni-O system, decreasing the amount of Fe below 0.67 also shifts the thermodynamics of oxygen exchange reaction in a favorable direction. The iron-poor material has higher magnitudes of both partial molar entropy and enthalpy. Similar to the Fe-Co-O system, the partial molar entropy is a less-strong function of oxygen content in the iron-poor Fe-Ni-O system.

3. Conclusions

In conclusion, we have explored various Fe-poor ferrites with lower Fe concentration than traditionally investigated spinel ferrites for two-step thermochemical CO_2 dissociation. We have also demonstrated a method that significantly improves the kinetics of both reaction steps, although requires further investigation. The Fe-poor composition not only lowers the ratio of redox active element, Fe, but also increases the rocksalt phase fraction; however, it counterintuitively increases the CO_2 dissociation capacity at condition of T_H = 1300°C and $CO:CO_2$ = 1:100 compared to spinel ferrites. Furthermore, we found the measured CO yield of $Fe_{0.35}Ni_{0.65}O_x$ is six times the thermodynamic equilibrium capacity of CeO_2, whereas La_1-

$_xSr_xMnO_{3-\delta}$ (x = 0.2, 0.3, 0.4) materials would have negative CO productions. We notice that while the Fe-poor ferrites have slower reaction kinetics than CeO_{2-X}, the thermodynamic CO_2 dissociation capacity is greatly improved, even when compared to other Fe-rich ferrites. CALPHAD thermodynamic models shed light on the general trend of CO_2 dissociation performance dependence on Fe concentration. Compared to traditional spinel ferrites, the Fe-poor ferrite system generally has significant portions of both rocksalt and spinel phases, and the ratio and composition of each phase change as oxygen exchange redox reactions proceed.

Acknowledgements

We would like to thank Adam S. Hoffman, Simon R. Bare and Professor Akbar Rhamdhani for their help in this work. This work was funded by the Department of Energy, Laboratory Directed Research and Development program at SLAC National Accelerator Laboratory, under contract DE-AC02-76SF00515. Additional support was provided by Stanford (SUNCAT and TomKat), by the Fuel Cell Technology Program in the Office of Energy Efficiency and Renewable Energy of the US Department of Energy and by the Office of Naval Research under grant N00014-17-1-2918. Use of the Stanford Synchrotron Radiation Lightsource, SLAC National Accelerator Laboratory, is supported by the U.S. Department of Energy, Office of Science, Office of Basic Energy Sciences under Contract No. DE-AC02-76SF00515. Part of this work was performed at the Stanford Nano Shared Facilities (SNSF).

Author Contributions

S.Z. and J.R. conceived the idea of using Fe-poor ferrites for thermochemical CO_2 dissociation and designed various sample compositions. A.M., W.C., I.J. and M.T. supervised the work. S.Z., J.R. and M.C. synthesized the samples. J.R. and S.Z. conducted CO_2 dissociation experiments in TGA system. S.Z. and C.X. performed SEM and EDS characterization. S.Z. and J.R. conducted quenching experiments. K.L. and S.Z. conducted XRD experiments and Rietveld refinement. S.Z., N.A. and M.C. conducted XANES characterization and data analysis. I.J. and J.R. conducted CALPHAD simulations. N.A., S.Z. and J.R. conducted thermodynamic analysis. S.Z. wrote the manuscript with contributions from all the authors.

Conflicts of interests

The authors declare no competing interests.

References

1 A. Majumdar, J. Deutch, S. Benson, R. Bras, E. Carter, D. Ort, M. Ramage, R. Socolow, E. Toone, G. Whitesides and M. Wrighton, 2016, 81.

2 A. Majumdar and J. Deutch, *Joule*, 2018, **2**, 805–809.

3 M. Joshi, E. Hawkins, R. Sutton, J. Lowe and D. Frame, *Nat. Clim. Chang.*, 2011, **1**, 407.

4 UNFCCC. Conference of the Parties (COP), *Paris Climate Change Conference-November 2015, COP 21*, 2015.

5 B. Walsh, P. Ciais, I. A. Janssens, J. Peñuelas, K. Riahi, F. Rydzak, D. P. van Vuuren and M. Obersteiner, *Nat. Commun.*, 2017, **8**, 14856.

6 N. MacDowell, N. Florin, A. Buchard, J. Hallett, A. Galindo, G. Jackson, C. S. Adjiman, C. K. Williams, N. Shah and P. Fennell, *Energy Environ. Sci.*, 2010, **3**, 1645–1669.

7 Y. Gao, X. Gao and X. Zhang, *Engineering*, 2017, **3**, 272–278.

8 S. Chu, Y. Cui and N. Liu, *Nat. Mater.*, 2016, **16**, 16.

9 T. Sakakura, J.-C. Choi and H. Yasuda, *Chem. Rev.*, 2007, **107**, 2365–2387.

10 Z. Jiang, T. Xiao, V. L. Kuznetsov and P. P. Edwards, *Philos. Trans. R. Soc. London A Math. Phys. Eng. Sci.*, 2010, **368**, 3343–3364.

11 W. Wang, S. Wang, X. Ma and J. Gong, *Chem. Soc. Rev.*, 2011, **40**, 3703–3727.

12 Q. Liu, L. Wu, R. Jackstell and M. Beller, *Nat. Commun.*, 2015, **6**, 5933.

13 M. D. Porosoff, B. Yan and J. G. Chen, *Energy Environ. Sci.*, 2016, **9**, 62–73.

14 M. Liu, Y. Pang, B. Zhang, P. De Luna, O. Voznyy, J. Xu, X. Zheng, C. T. Dinh, F. Fan, C. Cao, F. P. G. de Arquer, T. S. Safaei, A. Mepham, A. Klinkova, E. Kumacheva, T. Filleter, D. Sinton, S. O. Kelley and E. H. Sargent, *Nature*, 2016, **537**, 382.

15 D. D. Zhu, J. L. Liu and S. Z. Qiao, *Adv. Mater.*, 2016, **28**, 3423–3452.

16 L. Zhang, Z. Zhao and J. Gong, *Angew. Chemie Int. Ed.*, 2017, **56**, 11326–11353.

17 J. Qiao, Y. Liu, F. Hong and J. Zhang, *Chem. Soc. Rev.*, 2014, **43**, 631–675.

18 J. L. White, M. F. Baruch, J. E. Pander, Y. Hu, I. C. Fortmeyer, J. E. Park, T. Zhang,

K. Liao, J. Gu, Y. Yan, T. W. Shaw, E. Abelev and A. B. Bocarsly, *Chem. Rev.*, 2015, **115**, 12888–12935.

19 X. Chang, T. Wang and J. Gong, *Energy Environ. Sci.*, 2016, **9**, 2177–2196.

20 B. Kumar, M. Llorente, J. Froehlich, T. Dang, A. Sathrum and C. P. Kubiak, *Annu. Rev. Phys. Chem.*, 2012, **63**, 541–569.

21 J. Barber and P. D. Tran, *J. R. Soc. Interface*, , DOI:10.1098/rsif.2012.0984.

22 D. Kim, K. K. Sakimoto, D. Hong and P. Yang, *Angew. Chemie - Int. Ed.*, 2015, **54**, 3259–3266.

23 R. L. House, N. Y. M. Iha, R. L. Coppo, L. Alibabaei, B. D. Sherman, P. Kang, M. K. Brennaman, P. G. Hoertz and T. J. Meyer, *J. Photochem. Photobiol. C Photochem. Rev.*, 2015, **25**, 32–45.

24 T. Kodama and N. Gokon, *Chem. Rev.*, 2007, **107**, 4048–4077.

25 G. P. Smestad and A. Steinfeld, *Ind. Eng. Chem. Res.*, 2012, **51**, 11828–11840.

26 J. E. Miller, A. H. McDaniel and M. D. Allendorf, *Adv. Energy Mater.*, 2014, **4**, 1300469.

27 J. R. Scheffe and A. Steinfeld, *Mater. Today*, , DOI:10.1016/j.mattod.2014.04.025.

28 B. Xu, Y. Bhawe and M. E. Davis, *Proc. Natl. Acad. Sci.*, , DOI:10.1073/pnas.1206407109.

29 W. Li, H. Wang, X. Jiang, J. Zhu, Z. Liu, X. Guo and C. Song, *RSC Adv.*, 2018, **8**, 7651–7669.

30 W.-H. Wang, Y. Himeda, J. T. Muckerman, G. F. Manbeck and E. Fujita, *Chem. Rev.*, 2015, **115**, 12936–12973.

31 B. Meredig and C. Wolverton, *Phys. Rev. B - Condens. Matter Mater. Phys.*, 2009, **80**, 1–8.

32 W. C. Chueh, C. Falter, M. Abbott, D. Scipio, P. Furler, S. M. Haile and A. Steinfeld, *Science*, 2010, **330**, 1797–1801.

33 P. Furler, J. R. Scheffe and A. Steinfeld, *Energy Environ. Sci.*, 2012, **5**, 6098–6103.

34 P. Furler, J. Scheffe, M. Gorbar, L. Moes, U. Vogt and A. Steinfeld, *Energy & Fuels*, 2012, **26**, 7051–7059.

35 A. H. McDaniel, E. C. Miller, D. Arifin, A. Ambrosini, E. N. Coker, R. O'Hayre, W. C. Chueh and J. Tong, *Energy Environ. Sci.*, 2013, **6**, 2424–2428.

36 D. Marxer, P. Furler, M. Takacs and A. Steinfeld, *Energy Environ. Sci.*, 2017, **10**, 1142–1149.

37 R. J. Carrillo and J. R. Scheffe, *Sol. Energy*, 2017, **156**, 3–20.

38 A. Le Gal, S. Abanades, N. Bion, T. Le Mercier and V. Harlé, *Energy & Fuels*, 2013, **27**, 6068–6078.

39 S. Zhai, J. Rojas, N. Ahlborg, K. Lim, M. F. Toney, H. Jin, W. C. Chueh and A. Majumdar, *Energy Environ. Sci.*, 2018, **11**, 2172–2178.

40 M. Zinkevich, D. Djurovic and F. Aldinger, *Solid State Ionics*, 2006, **177**, 989–1001.

41 H. Tagawa, in *Proceedings of the 5th International Symposium on Solid Oxide Fuel Cells (SOFC-V)*, Aachen, Germany, 1997.

42 M. Oishi, K. Yashiro, K. Sato, J. Mizusaki and T. Kawada, *J. Solid State Chem.*, 2008, **181**, 3177–3184.

43 J. R. Scheffe, D. Weibel and A. Steinfeld, *Energy & Fuels*, 2013, **27**, 4250–4257.

44 M. Takacs, M. Hoes, M. Caduff, T. Cooper, J. R. Scheffe and A. Steinfeld, *Acta Mater.*, 2016, **103**, 700–710.

45 A. H. Bork, E. Povoden-Karadeniz and J. L. M. Rupp, *Adv. Energy Mater.*, 2017, **7**, 1601086.

46 M. Ezbiri, M. Takacs, D. Theiler, R. Michalsky and A. Steinfeld, *J. Mater. Chem. A*, , DOI:10.1039/c6ta06644e.

47 D. Romero Barcellos, M. D. Sanders, J. Tong, A. H. McDaniel and R. O'Hayre, *Energy Environ. Sci.*, , DOI:10.1039/C8EE01989D.

48 R. B. Diver, J. E. Miller, M. D. Allendorf, N. P. Siegel and R. E. Hogan, *J. Sol. Energy Eng.*, 2008, **130**, 041001.

49 T. Kodama, N. Gokon and R. Yamamoto, *Sol. Energy*, 2008, **82**, 73–79.

50 J. R. Scheffe, A. H. McDaniel, M. D. Allendorf and A. W. Weimer, *Energy Environ. Sci.*, 2013, **6**, 963–973.

51 J. Leonard, N. Reyes, K. M. Allen, K. Randhir, L. Li, N. AuYeung, J. Grunewald, N. Rhodes, M. Bobek and J. F. Klausner, *Int. J. Photoenergy*, ,

DOI:10.1155/2015/856385.

52 S. B. Han, T. B. Kang, O. S. Joo and K. D. Jung, *Sol. Energy*, 2007, **81**, 623–628.

53 J. R. Scheffe, J. Li and A. W. Weimer, *Int. J. Hydrogen Energy*, 2010, **35**, 3333–3340.

54 M. D. Allendorf, R. B. Diver, N. P. Siegel and J. E. Miller, *Energy & Fuels*, 2008, **22**, 4115–4124.

55 C. Jarrett, W. Chueh, C. Yuan, Y. Kawajiri, K. H. Sandhage and A. Henry, *Sol. Energy*, 2016, **123**, 57–73.

56 M. Ezbiri, M. Takacs, B. Stolz, J. Lungthok, A. Steinfeld and R. Michalsky, *J. Mater. Chem. A*, 2017, **5**, 15105–15115.

57 T. Nakamura, K. Yashiro, K. Sato and J. Mizusaki, *Solid State Ionics*, 2009, **180**, 368–376.

58 C. L. Muhich, S. Blaser, M. C. Hoes and A. Steinfeld, *Int. J. Hydrogen Energy*, 2018, **43**, 18814–18831.

59 M. E. Gálvez, P. G. Loutzenhiser, I. Hischier and A. Steinfeld, *Energy and Fuels*, 2008, **22**, 3544–3550.

60 A. Stamatiou, P. G. Loutzenhiser and A. Steinfeld, *Energy and Fuels*, 2010, **24**, 2716–2722.

61 A. Tofighi and F. Sibieude, *Int. J. Hydrogen Energy*, 1984, **9**, 293–296.

62 A. Steinfeld, S. Sanders and R. Palumbo, *Sol. Energy*, 1999, **65**, 43–53.

63 H. Aoki, H. Kaneko, N. Hasegawa, H. Ishihara, Y. Takahashi, A. Suzuki and Y. Tamaura, in *ASME International Solar Energy Conference, Solar Energy*, 2004, pp. 515–517.

64 H. Aoki, H. Kaneko, N. Hasegawa, H. Ishihara, A. Suzuki and Y. Tamaura, *Solid State Ionics*, 2004, **172**, 113–116.

65 H. Ishihara, N. Hasegawa, H. Aoki, H. Kaneko, A. Suzuki and Y. Tamaura, *Solid State Ionics*, 2004, **172**, 117–119.

66 K. Ehrensberger, P. Kuhn, V. Shkloverb and H. Oswald, *Solid State Ionics*, 1996, **90**, 75–81.

67 T. Kodama, T. Shimizu, T. Satoh, M. Nakata and K. I. Shimizu, *Sol. Energy*, 2002, **73**, 363–374.

68 N. Gokon, T. Mizuno, Y. Nakamuro and T. Kodama, *J. Sol. Energy Eng.*, 2007, **130**, 11016–11018.

69 H. Ishihara, H. Kaneko, T. Yokoyama, A. Fuse, N. Hasegawa and Y. Tamaura, in *ASME. International Solar Energy Conference, Solar Energy*, 2005, pp. 687–689.

70 T. Kodama, Y. Nakamuro and T. Mizuno, *J. Sol. Energy Eng.*, 2004, **128**, 3–7.

71 Y. Tamaura, A. Steinfeld, P. Kuhn and K. Ehrensberger, *Energy*, 1995, **20**, 325–330.

72 T. A. S. Ferreira, J. C. Waerenborgh, M. H. R. M. Mendonça, M. R. Nunes and F. M. Costa, *Solid State Sci.*, 2003, **5**, 383–392.

73 S. G. Mohamed, C. J. Chen, C. K. Chen, S. F. Hu and R. S. Liu, *ACS Appl. Mater. Interfaces*, 2014, **6**, 22701–22708.

74 D. Santos-Carballal, A. Roldan, R. Grau-Crespo and N. H. De Leeuw, *Phys. Rev. B - Condens. Matter Mater. Phys.*, 2015, **91**, 195106.

75 R. J. Panlener, R. N. Blumenthal and J. E. Garnier, *J. Phys. Chem. Solids*, 1975, **36**, 1213–1222.

Figures and Captions

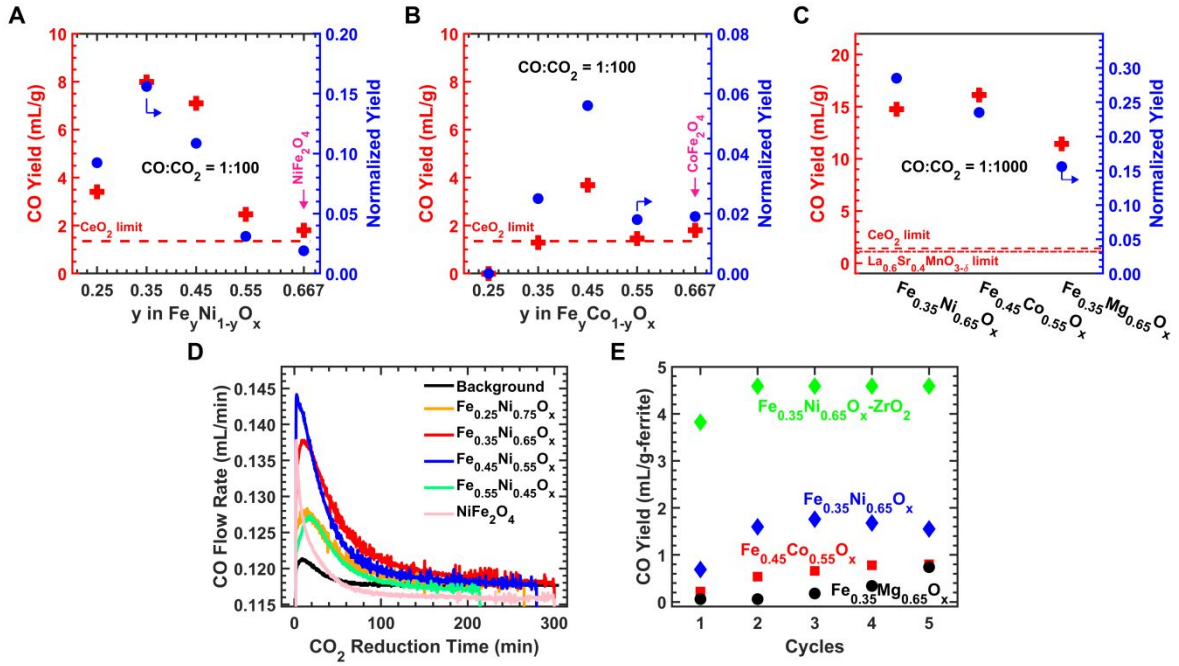

Fig. 1 | Improved performance of Fe-poor ferrites in two-step thermochemical CO_2 dissociation experiments. A and **B**, CO yield of $Fe_yNi_{1-y}O_x$ and $Fe_yCo_{1-y}O_x$. Reaction conditions were: (1) thermal reduction under T_H = 1300°C and pO_2 = 10 ppm for 5 hours, (2) CO_2 splitting under T_L = 800°C and background gas partial pressure $CO:CO_2$ = 1:100 for 5 hours. "Normalized yield" was derived by dividing measured CO yield by "Fe redox limit" (see main text). Thermodynamic equilibrium CO yield of CeO_2 was indicated by dash line. **C**, CO yield of $Fe_{0.35}Ni_{0.65}O_x$, $Fe_{0.45}Co_{0.55}O_x$ and $Fe_{0.35}Mg_{0.65}O_x$, with the same reaction conditions as **A** and **B** except that $CO:CO_2$ was 1:1000. Thermodynamic equilibrium CO yields of CeO_2 and $La_{0.6}Sr_{0.4}MnO_{3-\delta}$ were indicated by different dash lines. **D**, CO concentration profiles using $Fe_yNi_{1-y}O_x$. "Background" indicates a test of background CO concentration without sample. Reaction conditions were the same as **A** and **B**. **E**, improvement of kinetics by ZrO_2. Multi-cycle thermochemical CO_2 dissociation experiments were performed using $Fe_{0.35}Ni_{0.65}O_x$, $Fe_{0.45}Co_{0.55}O_x$, $Fe_{0.35}Mg_{0.65}O_x$ and $Fe_{0.35}Ni_{0.65}O_x$-ZrO_2. With limited reaction time (1 hour each step), the addition of ZrO_2 (80% mass fraction) shows a significant improvement in the CO yield per gram of ferrite. Reaction conditions

were the same as **A** and **B** except reaction time. All measured CO yields had uncertainty of ± 0.2 mL-CO/g/hour due to CO sensor drift. Sample masses were about 0.13 g.

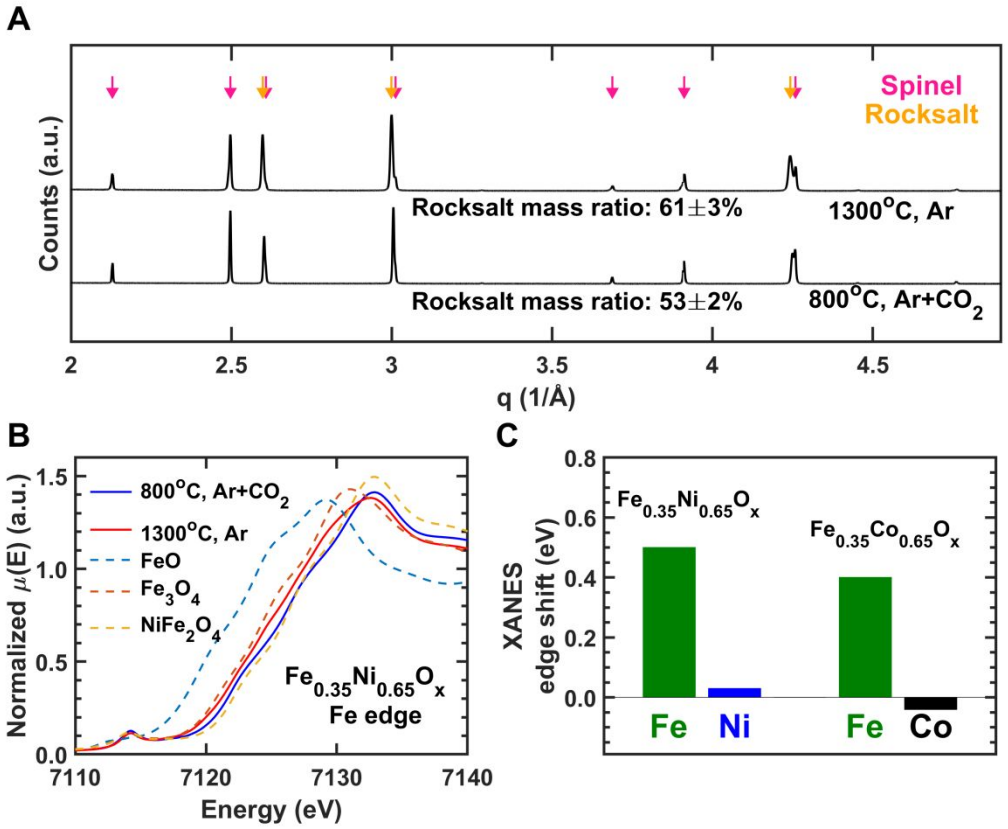

Fig. 2 | X-ray characterizations of quenched Fe-poor ferrite $Fe_{0.35}Ni_{0.65}O_x$. Quenching conditions are T_H = 1300°C in argon, and T_L = 800°C in 20% CO_2 balance argon. **A**, X-ray diffraction $Fe_{0.35}Ni_{0.65}O_x$; rocksalt phase mass ratio is from Rietveld refinement. **B**, Fe K edge x-ray absorption near edge structure (XANES) of $Fe_{0.35}Ni_{0.65}O_x$, as well as reference oxides. **C**. XANES edge shift was evaluated at normalized absorption of 0.5.

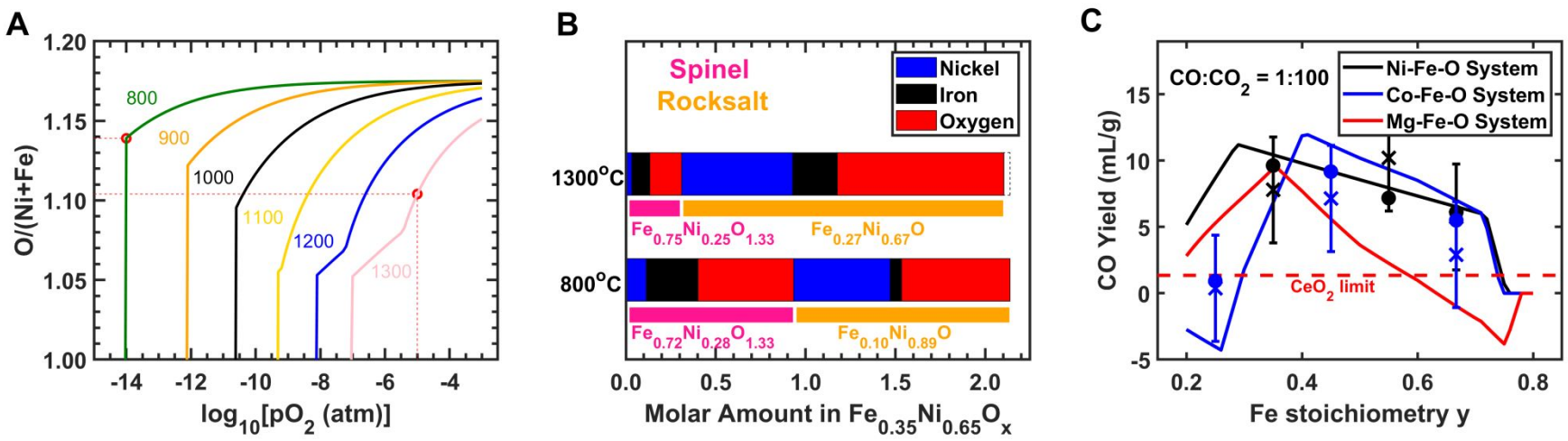

Fig. 3 | Thermodynamics of $Fe_yNi_{1-y}O_x$ from CALPHAD simulation and long cycle measurements. A, $Fe_{0.35}Ni_{0.65}O_x$ oxygen stoichiometry dependence on oxygen partial pressure (pO_2) at various temperatures (unit: °C) from CALPHAD; two circles indicate T_H = 1300°C with pO_2 = 10 ppm, and T_L = 800°C with $pO_2 = 10^{-14}$ atm. **B**, elemental composition of rocksalt and spinel phases for $Fe_{0.35}Ni_{0.65}O_x$ at conditions of 1300°C with pO_2 = 10 ppm, and 800°C and $pO_2 = 10^{-14}$ atm. The total molar amount of cations is unity. Dash line shows the difference in length due to oxygen amount difference. **C**, equilibrium CO yield from $Fe_yM_{1-y}O_x$ system (M = Mg, Co, Ni); reaction conditions are: (1) thermal reduction under T_H = 1300°C and pO_2 = 10 ppm, (2) CO_2 splitting under T_L = 800°C and with gas ratio $CO:CO_2$=1:100. Experimental results for $Fe_yNi_{1-y}O_x$ and $Fe_yCo_{1-y}O_x$ materials from TGA system (20 hours dwelling for each step) are indicated by cross (CO sensor derived, ± 4.0 mL-CO/g)

and dot (thermogravimetry derived).

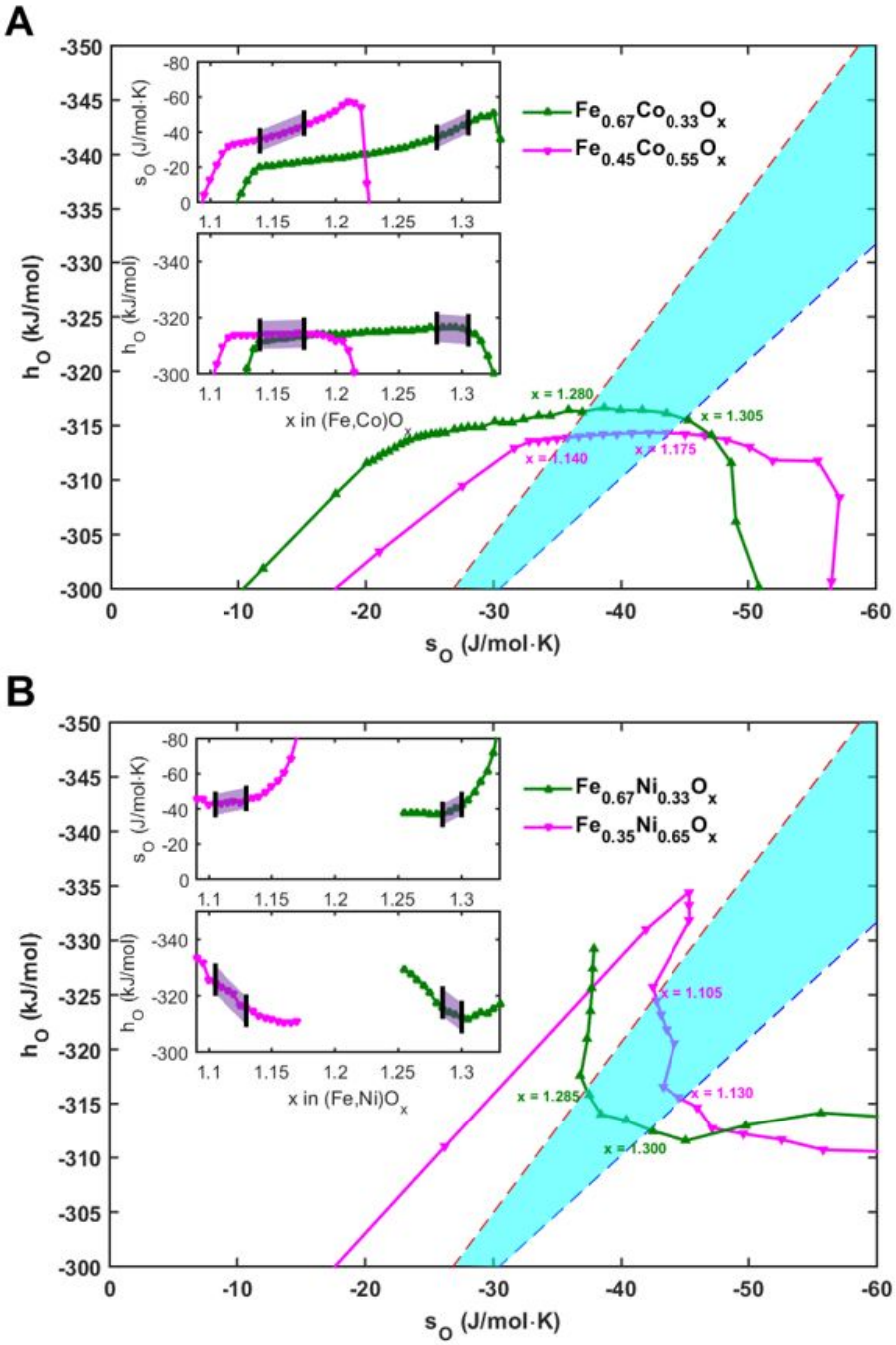

Fig. 4 | Thermodynamic selectivity plots for cobalt ferrites (A) and nickel ferrites (B). The red dashed line represents thermodynamic equilibrium for T_H = 1300°C with pO_2 = 10 ppm. The blue dashed line represents equilibrium for T_L = 800°C with $CO:CO_2$ = 1:100. Calculated partial molar quantities for ferrites from CALPHAD are shown as lines with symbols, such that each line segment represents 0.005 mole of oxygen change, namely, 0.005 change of x.

Tables and Captions

Table 1. Thermodynamic equilibrium CO yield for state-of-the-art materials (mL-CO/g). Thermal reduction is set at T_H and pO_2 = 10 ppm, and CO_2 splitting step is set at T_L = 800°C and CO_2:CO = 100:1. Ferrite results are from CALPHAD simulation. Negative CO yield means that CO_2 dissociation is not thermodynamically favored.

T_H (°C)	CeO_2[40,58,75]	$La_{0.7}Sr_{0.3}MnO_{3-\delta}$[45]	$La_{0.6}Sr_{0.4}MnO_{3-\delta}$[45]	$Fe_{0.35}Ni_{0.65}O_x$
1100	0.05	-5.47	-11.64	-6.84
1200	0.40	-4.76	-9.11	-1.59
1300	1.34	-2.73	-5.47	10.43
1400	3.73	0.00	-1.62	20.20
1500	8.08	3.44	1.62	25.20